Available online at www.sciencedirect.com
SCIENCE DIRECT®
Comput. Methods Appl. Mech. Engrg. 193 (2004) 1645–1669
Computer methods in applied mechanics and engineering
www.elsevier.com/locate/cma

A bridging domain method for coupling continua with molecular dynamics

S.P. Xiao [a], T. Belytschko [b,*]

[a] Department of Mechanical and Industrial Engineering and Center for Computer-Aided Design, 3131 Seamans Center, University of Iowa, Iowa City, IA 52242, USA
[b] Department of Mechanical Engineering, 2145 N Sheridan Road, Northwestern University, Evanston, IL 60208-3111, USA

Received 19 May 2003; received in revised form 9 October 2003; accepted 2 December 2003

Abstract

A bridging domain method for coupling continuum models with molecular models is described. In this method, the continuum and molecular domains are overlapped in a bridging subdomain, where the Hamiltonian is taken to be a linear combination of the continuum and molecular Hamiltonians. We enforce the compatibility in the bridging domain by Lagrange multipliers or by the augmented Lagrangian method. An explicit algorithm for dynamic solutions is developed. Results show that this multiscale method can avoid spurious wave reflections at the molecular/continuum interface without any additional filtering procedures, even for problems with significant nonlinearities. The method is also shown to naturally handle the coupling of the continuum energy equation with the molecular subdomain. A multiple-time-step algorithm is also developed within this framework.

Keywords: Molecular dynamics; Fracture; Multiscale methods; Heat transfer; Spurious wave reflection

1. Introduction

Concurrent methods for coupling molecular dynamics models with continuum or quasicontinuum [1] models are useful for studying local phenomena such as fracture. They permit the use of far fewer equations than in strict molecular dynamics models, since the resolution in the subdomain modeled by continuum mechanics can be far coarser than in the molecular dynamics model. In these coupled models, the continuum subdomain serves primarily as a boundary model that provides the low frequency impedance and a sink for the energy associated with outgoing waves of the molecular dynamics model. Such models are often called multiscale because the spectra (and the resolution) of the continuum model have much smaller cutoff frequencies than the molecular dynamics model.

* Corresponding author. Tel.: +1-847-491-4029; fax: +1-847-491-4011.
E-mail address: tedbelytschko@northwestern.edu (T. Belytschko).

0045-7825/$ - see front matter © 2004 Elsevier B.V. All rights reserved.
doi:10.1016/j.cma.2003.12.053

A difficulty that arises in such concurrent multiscale couplings is that the high frequency parts of waves are often spuriously reflected at the molecular/continuum interface; this phenomenon was already noted by Doll and Adelman [2,3]. It was also noted in finite element models with different element sizes by Holmes and Belytschko [4]. These spurious reflections can be explained by noting that for a wave with a frequency greater than the cutoff frequency of the continuum model, the interface appears as an almost rigid boundary. So instead of smoothly propagating into the continuum model, the high frequency part of the wave is reflected. This results in spurious growth of energy in the molecular domain.

Recently, several concurrent multiscale techniques have been developed; we will briefly review some of these works. Abraham et al. [5,6], in a pioneering work, developed a methodology that couples a tight-binding quantum mechanics approximation with molecular dynamics and in turn with a finite element continuum model. The molecular dynamics model was coupled with the continuum model in a "handshake" domain in which the two Hamiltonians were averaged. To reduce spurious reflections into the molecular dynamics domain, damping was used in the handshake region, although the damping was not based on any rigorous theory. In most cases, it appears that the finite element continuum model had to be nearly of the scale of interatomic distances at the atomistic/continuum interface to perform well.

In a significant advance, Rudd and Broughton [7] formulated a coarse-grained method. In this method, the fine scale response was modeled in the coarse scale domain by superimposing the atomistic Hamiltonian. For purposes of tractability, the Hamiltonian employed a linearization of the potential energy. The fine scale effects were then computed by taking advantage of Bloch symmetry to reduce the size of the dynamic matrix. Their results exhibit excellent phonon spectra and minimal reflection of elastic waves between subdomains, although the results were given only for one-dimensional models.

Wagner and Liu [8] have developed a multiscale method in which the molecular displacements are decomposed into fine and coarse scales throughout the domain. However, in the coarse scale domain the fine scale features are not modeled explicitly. At the interface between the two domains, they use a form of the Langevin equation to eliminate spurious reflections. They reported excellent results for one-dimensional problems.

Cai et al. [9] introduced a condensation approach to minimize boundary wave reflection. However, it requires the calculation of response functions, which take the form of matrices of size equal to the number of degrees of freedom along the boundary of the MD domain. These matrices are computed by MD simulations on domains somewhat larger than the one of interest.

E and Huang [10] have developed nonreflecting interfaces by constructing time integration formulas that eliminate spurious reflections. The method is based on eliminating the high frequency components moving from fine mesh to coarse mesh. As with most of the previous work, the reported examples were limited to one-dimensional linear systems.

Karpov et al. [11] have developed coupling methods based on lattice dynamics. As in [7,8], the molecular displacements are modeled as the sum of a coarse scale (represented by finite element interpolants) and a fine scale. In the continuum domain, only a finite element model is used. The spurious reflections at the edge of the molecular model are eliminated by introducing forces equivalent to the lattice impedance; this entails the evaluation of inverse Laplace transforms in time, and for multidimensional problems, a Fourier transform in space. The method is very effective for linear continua, but the extension to nonlinear response may be difficult.

Belytschko and Xiao [12] have developed a coupling method for molecular mechanics (we refer to molecular models at zero temperature as molecular mechanics) and continuum mechanics models based on a bridging domain method. In this method, the two domains are overlaid at the interface as in the method described here. A scaling of the fine and coarse scale potential is used in conjunction with Lagrange multipliers on the overlapping subdomain.

A review of these methods can be found in [13]. It should be noted that in multiscale analysis, it is beneficial if in the time integration of the system, the time step in the continuum subdomain be much larger than in the atomistic subdomain. Mixed time integration procedures, where different time steps are used in different subdomains, have already been extensively developed in the finite element community [14–17]. However, in the finite element community, these integrators were developed without considering the mitigation of spurious reflections between subdomains. The challenge is to combine the stability properties of these integrators with techniques that minimize spurious reflections that may arise due to the disparity in time steps.

A coupling method called the bridging domain method is developed in this paper. It is an extension of the method in [12] to dynamics. The method was previously used to couple finite elements to meshless methods in [18]. It has been studied by Ben Dhia [19]. In this method, the molecular model and continuum model overlap at their junctions in a bridging domain. This method can avoid spurious wave reflection without any additional filtering or damping. In effect, the method projects the fine scale solution onto the coarse scale solution in the bridging domain at each time step. Thus it filters the high frequency components at the interface. Since the positions of atoms and nodes are not necessarily identical in the bridging domain, a uniform mesh can be used in continuum subdomain and the continuum mesh need not correspond with atomic positions. In addition, multiple time steps can be implemented into this method for different length scales. Furthermore, since the method is not based on linearization, it was surmised that it would apply to nonlinear problems. Based on the test problems we have studied so far, this appears to be the case.

The method also provides a natural way to couple heat conduction and other diffusion phenomena between molecular and continuum models. Temperature and other diffusion variables can only be defined in a molecular model over a subdomain containing an adequate number of atoms, so edge-to-edge couplings are impossible. In the proposed method, the temperature in the domain adjacent to the overlapping molecular domain is used to drive the energy transfer between the molecular and continuum models. A switch is included so that the second law of thermodynamics is not violated.

The outline of this paper is as follows: In Section 2, we describe the governing equations. The Hamiltonian dynamics of both the molecular and the continuum models are presented. In Section 3, the bridging domain coupling method is developed. The coupling method is set up first and the discrete equations are derived for both the Lagrange multiplier method and the augmented Lagrangian method. An explicit algorithm for dynamics solutions and multiple-time-step algorithms are described. Then we briefly describe the treatment of heat conduction with the bridging domain coupling method. In Section 5, applications of multiscale methods in 1D and 2D are studied. Section 6 gives the conclusions.

2. Governing equations

The model for the bridging domain coupling method is shown in Fig. 1. The complete domain in the initial configuration is denoted by Ω_0. The domain is subdivided into two subdomains: the molecular subdomain denoted by Ω_0^{M}, and the continuum subdomain, denoted by Ω_0^{C}. The overlap of these two domains is denoted by Ω_0^{int} in the initial configuration; Ω_0^{int} is called the bridging domain and it corresponds to the overlap of the two subdomains; Γ_0^{α} denotes the edges of the continuum subdomains and Γ_1^{α} denotes the edges of the molecular subdomain.

2.1. Molecular/atomistic model

In an isolated system of atoms or molecules, the total energy, the sum of the kinetic and potential energies of the molecules, is constant in time and identified as the Hamiltonian H^{M}, which is given by

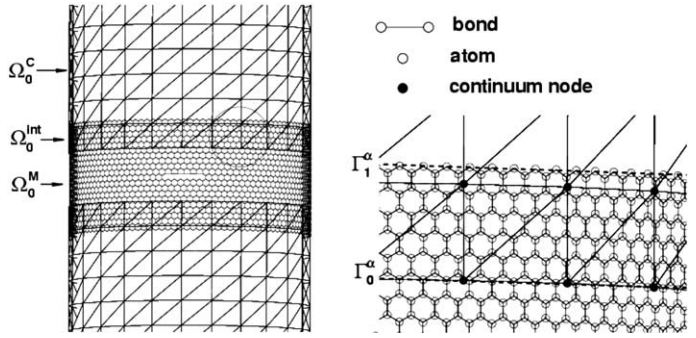

Fig. 1. Bridging domain model for a nanotube; finite elements are indicated by lines that connect continuum nodes.

$$H^{\mathrm{M}}(\mathbf{x}_I(t), \mathbf{p}_I^{\mathrm{M}}(t)) = \sum_I \frac{1}{2m_I}\mathbf{p}_I^{\mathrm{M}} \cdot \mathbf{p}_I^{\mathrm{M}} + W^{\mathrm{M}}(\mathbf{x}_I(t)) = \text{constant}, \tag{1}$$

where m_I is the mass of atom I, $\mathbf{x}_I$ is the position of atom I and $\mathbf{x}_I = \mathbf{X}_I + \mathbf{d}_I$ ($\mathbf{X}_I$ is the original position of atom I and $\mathbf{d}_I$ is the displacement of atom I); $\mathbf{p}_I^{\mathrm{M}}$ is the momentum and defined by

$$\mathbf{p}_I^{\mathrm{M}} = m_I\dot{\mathbf{x}}_I = m_I\dot{\mathbf{d}}_I. \tag{2}$$

$W^{\mathrm{M}}(\mathbf{x})$ is the potential function which is the sum of the energies due to any force fields, such as pair-wise interaction of the atoms, three-body potentials or others. It can be written as

$$W^{\mathrm{M}}(\mathbf{x}_I) = \sum_I W_1(\mathbf{x}_I) + \sum_{I,J>I} W_2(\mathbf{x}_I, \mathbf{x}_J) + \sum_{I,J>I,K>J} W_3(\mathbf{x}_I, \mathbf{x}_J, \mathbf{x}_K) + \cdots \tag{3}$$

Here, we assume that the external potential is due only to a constant external force, $\mathbf{f}_I^{\mathrm{ext}}$, such as electrostatic forces, and a pair-wise interatomic potential denoted by $w_{IJ} = w_{\mathrm{M}}(\mathbf{x}_I, \mathbf{x}_J)$, so the total potential is

$$W^{\mathrm{M}} = -W_{\mathrm{M}}^{\mathrm{ext}} + W_{\mathrm{M}}^{\mathrm{int}} = -\sum_I \mathbf{f}_I^{\mathrm{ext}}\mathbf{d}_I + \sum_{I,J>I} w_{\mathrm{M}}(\mathbf{x}_I, \mathbf{x}_J). \tag{4}$$

The well-known Hamiltonian canonical equations of motion are

$$\dot{\mathbf{p}}_I^{\mathrm{M}} = -\frac{\partial H}{\partial \mathbf{x}_I} = -\frac{\partial W^{\mathrm{M}}}{\partial \mathbf{x}_I}, \quad \dot{\mathbf{x}}_I = \dot{\mathbf{d}}_I = \frac{\partial H}{\partial \mathbf{p}_I^{\mathrm{M}}} = \frac{\mathbf{p}_I^{\mathrm{M}}}{m_I}. \tag{5}$$

Eq. (5) can be combined to yield

$$m_I\ddot{\mathbf{d}}_I = -\frac{\partial W^{\mathrm{M}}}{\partial \mathbf{x}_I} = \frac{\partial W_{\mathrm{M}}^{\mathrm{ext}}}{\partial \mathbf{d}_I} - \frac{\partial W_{\mathrm{M}}^{\mathrm{int}}}{\partial \mathbf{d}_I} = \mathbf{f}_I^{\mathrm{ext}} - \mathbf{f}_I^{\mathrm{int}}, \tag{6}$$

where $\mathbf{f}_I^{\mathrm{int}} = \partial W_{\mathrm{M}}^{\mathrm{int}}/\partial \mathbf{d}_I$.

2.2. Continuum model

We will adopt a Lagrangian viewpoint for the continuum. This presupposes that any atoms in the domain that is to be treated by continuum methods remain in that domain. Thus our methods are not directly applicable to gases or even solid behavior characterized by diffusion of atoms. Our method is aimed at crystalline or amorphous solids, and it is assumed that the deformations are sufficiently small so that voids or dislocations do not develop in the continuum subdomain. However, the method could be extended to treat the latter.

The continuum is governed by the conservation of mass, linear and angular momentum and energy; closure is provided by the constitutive equations. The mass conservation equation for a Lagrangian description is an algebraic equation (see [20]) from which the density can be computed, so we will ignore it here.

The linear momentum equations are

$$\frac{\partial P_{ji}}{\partial X_j} + \rho_0 b_i = \rho_0 \ddot{u}_i, \tag{7}$$

where ρ_0 is the initial density, $\mathbf{P}$ is the first Piola–Kirchhoff stress tensor, $\mathbf{b}$ is the body force per unit mass and $\mathbf{u}$ is the displacement, superposed dots denote material time derivatives. The first Piola–Kirchhoff stress can be obtained from the potential of the continuum by

$$\mathbf{P} = \frac{\partial w_{\mathrm{C}}(\mathbf{F})}{\partial \mathbf{F}}, \tag{8}$$

where $\mathbf{F}$ is the deformation gradient and w_{C} is the potential energy per unit volume of the continuum. The potential energy depends on the elongations and angle changes of the atomic bonds that underlie the continuum model. The above serves as the constitutive equation for a continuum based on atomistic potentials. The total potential of the continuum model is defined by

$$W_{\mathrm{C}}^{\mathrm{int}} = \int_{\Omega_0^{\mathrm{C}}} w_{\mathrm{C}}(\mathbf{F})\, \mathrm{d}\Omega_0^{\mathrm{C}}. \tag{9}$$

The constitutive equation is constructed via the Cauchy–Born rule by the quasicontinuum approach. For curved monolayer crystalline membranes such as nanotubes, an extension of the Cauchy–Born rule called the exponential Cauchy–Born rule is used, see [22].

We assume Fourier's law for heat conduction, so the energy equation is

$$\rho \bar{c} \dot{T} = \sigma_{ij} v_{i,j} + \kappa \nabla^2 T + S, \tag{10}$$

where T is the temperature, S is the internal heat source, $\bar{c}$ is the specific heat, and κ is the conductivity. We assume that all deformations are reversible, so no conversion of the first term on the right hand side to heat takes place. At the scale of 10–100 nm, the effects of heat waves may become important, see for example, [23]. However, we will neglect these effects here.

The system must also conform to the second law of thermodynamics. Within the context of the processes we are considering here, the second law is observed if the material law meets the Clausius–Planck inequality and if heat flows in the direction of the negative thermal gradient. The latter condition is automatically met in the continuum when $\kappa > 0$. In the overlapping subdomain, the second law requires that we permit heat to flow from the molecular model to the continuum only when the temperature in the linked cell of the molecular model is greater than the temperature at the corresponding point in the continuum model.

In the continuum domain, the Hamiltonian is given by

$$H^{\mathrm{C}} = K^{\mathrm{C}} + W^{\mathrm{C}} = \int_{\Omega_0^{\mathrm{C}}} \frac{1}{2} \rho \mathbf{v}^{\mathrm{T}} \mathbf{v}\, \mathrm{d}\Omega_0^{\mathrm{C}} + W^{\mathrm{C}}, \tag{11}$$

$$W^{\mathrm{C}} = -W_{\mathrm{C}}^{\mathrm{ext}} + W_{\mathrm{C}}^{\mathrm{int}} = -\sum_I \mathbf{f}_I^{\mathrm{ext\,C}} \mathbf{u}_I + \int_{\Omega_0^{\mathrm{C}}} w_{\mathrm{C}}(\mathbf{F})\, \mathrm{d}\Omega_0^{\mathrm{C}}. \tag{12}$$

Note that we use the same symbol for the nodal forces for the continuum model once it is discretized by a finite element method. The velocity in the continuum $\mathbf{v}(\mathbf{X}, t)$ is approximated by

$$\mathbf{v}(\mathbf{X}, t) = \sum_I N_I(\mathbf{X}) \mathbf{v}_I(t) \quad \text{or} \quad v_i(\mathbf{X}, t) = \sum_I N_I(\mathbf{X}) v_{iI}(t), \tag{13}$$

where $N_I(\mathbf{X})$ are the shape functions. The following discrete equations are then obtained:

$$M_I \ddot{u}_{iI} = f_{iI}^{\text{ext C}} - f_{iI}^{\text{int C}}, \quad M_I = \rho_0 V_I^0, \tag{14}$$

where M_I is the lumped mass of node I; $f_{iI}^{\text{ext C}}$ and $f_{iI}^{\text{int C}}$ are the external and internal nodal forces respectively, given by

$$f_{iI}^{\text{ext C}} = \frac{\partial W_{\text{C}}^{\text{ext}}}{\partial X_{iI}}, \tag{15}$$

$$f_{iI}^{\text{int C}} = \int_{\Omega_0^{\text{C}}} \frac{\partial N_I(\mathbf{X})}{\partial X_j} \frac{\partial w_{\text{C}}(\mathbf{F})}{\partial F_{ij}} \, \mathrm{d}\Omega_0^{\text{C}} = \int_{\Omega_0^{\text{C}}} \frac{\partial N_I(\mathbf{X})}{\partial X_j} P_{ji} \, \mathrm{d}\Omega_0^{\text{C}} = \int_{\Omega^{\text{C}}} \frac{\partial N_I(\mathbf{x})}{\partial x_j} \sigma_{ji} \, \mathrm{d}\Omega^{\text{C}}, \tag{16}$$

where Ω is the current domain, see [20] for details.

3. Bridging domain coupling method

3.1. Coupling method

In the bridging domain method, the total energy is taken to be a linear combination of the molecular and continuum energies. A scaling parameter α is introduced in the bridging subdomain, i.e. the overlapping subdomain. The parameter α is defined as $\alpha = \frac{l(\mathbf{X})}{l_0}$ where $l(\mathbf{X})$ is the orthogonal projection of $\mathbf{X}$ onto Γ_0^α and l_0 is the length of this orthogonal projection to Γ_1^α as shown in Fig. 2. Therefore, the parameter α is

$$\alpha = \begin{cases} 1 & \text{in } \Omega_0^{\text{C}} - \Omega_0^{\text{int}}, \\ [0,1] & \text{in } \Omega_0^{\text{int}}, \\ 0 & \text{in } \Omega_0^{\text{M}} - \Omega_0^{\text{int}}. \end{cases} \tag{17}$$

The overlapping domain must be quite regular for the above definition of the scaling to be well defined.

The Hamiltonian for the complete domain is taken to be a linear combination of the molecular and continuum Hamiltonians

$$H = (1-\alpha)H^{\text{M}} + \alpha H^{\text{C}} = \sum_I (1 - \alpha(\mathbf{X}_I)) \frac{\mathbf{p}_I^{\text{M}} \cdot \mathbf{p}_I^{\text{M}}}{2m_I} + (1-\alpha)W^{\text{M}} + \sum_I \alpha(\mathbf{X}_I) \frac{\mathbf{p}_I^{\text{C}} \cdot \mathbf{p}_I^{\text{C}}}{2M_I} + \alpha W^{\text{C}}, \tag{18}$$

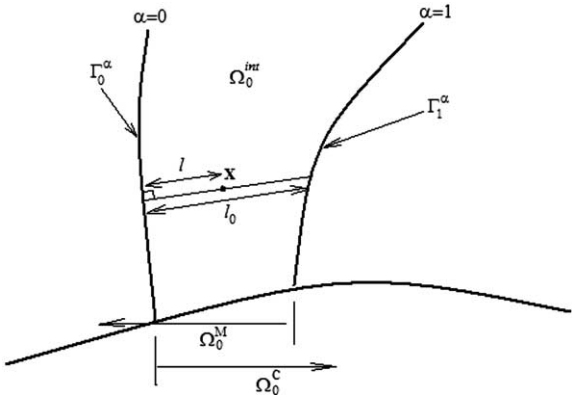

Fig. 2. Bridging domain between continuum and molecular model.

where W^{M} is defined in (4) and W^{C} in (9). The two models are constrained on the overlapping subdomain Ω_0^{int} by

$$\mathbf{g}_I = \{g_{iI}\} = \{u_i(\mathbf{X}_I) - d_{iI}\} = \left\{ \sum_J N_J(\mathbf{X}_I) u_{iJ} - d_{iI} \right\} = 0, \tag{19}$$

i.e. the atomic displacements are required to conform to the continuum displacements at the positions of the atoms. The constraints are applied to all components of the displacements.

We first show how the constraint is applied by the Lagrange multiplier method; we then add the modifications needed for the augmented Lagrangian method. In the Lagrange multiplier method, the total Hamiltonian is written as

$$H_{\mathrm{L}} = H + \boldsymbol{\lambda}^{\mathrm{T}}\mathbf{g} = H + \sum_I \boldsymbol{\lambda}_I^{\mathrm{T}}\mathbf{g}_I, \tag{20}$$

where $\boldsymbol{\lambda}_I = \{\lambda_{iI}\}$ is a vector of Lagrange multipliers whose components correspond to the components of the displacement of atom I. Note that the Lagrange multipliers are assigned to the discrete positions of atoms.

The augmented Lagrangian method can be developed by adding a penalty to (20). The total Hamiltonian is then

$$H_{\mathrm{AL}} = H + \boldsymbol{\lambda}^{\mathrm{T}}\mathbf{g} + \frac{1}{2}\beta\mathbf{g}^{\mathrm{T}}\mathbf{g} = H + \sum_I \boldsymbol{\lambda}_I^{\mathrm{T}}\mathbf{g}_I + \frac{1}{2}\sum_I \beta\mathbf{g}_I^{\mathrm{T}}\mathbf{g}_I, \tag{21}$$

where β is penalty parameter.

3.2. Discrete equations

The equations of motion for the Lagrange multiplier method are

$$\alpha(\mathbf{X}_I)\dot{\mathbf{p}}_I^{\mathrm{C}} = -\frac{\partial H_{\mathrm{L}}}{\partial \mathbf{u}_I}, \quad \alpha(\mathbf{X}_I)\dot{\mathbf{u}}_I = \frac{\partial H_{\mathrm{L}}}{\partial \mathbf{p}_I^{\mathrm{C}}} \qquad \text{in } \Omega_0^{\mathrm{C}}, \tag{22}$$

$$(1-\alpha(\mathbf{X}_I))\dot{\mathbf{p}}_I^{\mathrm{M}} = -\frac{\partial H_{\mathrm{L}}}{\partial \mathbf{d}_I}, \quad (1-\alpha(\mathbf{X}_I))\dot{\mathbf{d}}_I = \frac{\partial H_{\mathrm{L}}}{\partial \mathbf{p}_I^{\mathrm{M}}} \qquad \text{in } \Omega_0^{\mathrm{M}}. \tag{23}$$

These can be combined to yield

$$\begin{aligned} &\overline{M}_I\ddot{\mathbf{u}}_I = \mathbf{f}_I^{\mathrm{ext\,C}} - \mathbf{f}_I^{\mathrm{int\,C}} - \mathbf{f}_I^{\mathrm{LC}} \quad \text{in } \Omega_0^{\mathrm{C}}, \\ &\bar{m}_I\ddot{\mathbf{d}}_I = \mathbf{f}_I^{\mathrm{ext}} - \mathbf{f}_I^{\mathrm{int}} - \mathbf{f}_I^{\mathrm{L}} \quad \text{in } \Omega_0^{\mathrm{M}}, \end{aligned} \tag{24}$$

where

$$\overline{M}_I = \alpha(\mathbf{X}_I)M_I, \quad \bar{m}_I = (1-\alpha(\mathbf{X}_I))m_I.$$

The external nodal forces including the scaling factor are defined to be

$$\begin{aligned} &\mathbf{f}_I^{\mathrm{ext\,C}} = \int_{\Omega_0^{\mathrm{C}}} \alpha(\mathbf{X}) N_I \rho_0 \mathbf{b}\, \mathrm{d}\Omega_0^{\mathrm{C}} + \int_{\Gamma_0^t} \alpha(\mathbf{X}) N_I \bar{\mathbf{t}}\, \mathrm{d}\Gamma_0^t, \\ &\mathbf{f}_I^{\mathrm{ext}} = (1-\alpha(X_I))\bar{\mathbf{f}}_I. \end{aligned} \tag{25}$$

Similarly, the internal forces are

$$\mathbf{f}_I^{\mathrm{int\,C}} = \int_{\Omega_0^{\mathrm{C}}} \alpha(\mathbf{X}) \frac{\partial N_I(\mathbf{X})}{\partial X_j} P_{ji}\, \mathrm{d}\Omega_0^{\mathrm{C}}, \tag{26}$$

$$\mathbf{f}_I^{\text{int}} = (1-\alpha(\mathbf{X}_I))\sum_{I,J>I}\frac{\partial w_{\text{M}}(\mathbf{x}_I,\mathbf{x}_J)}{\partial \mathbf{d}_I}. \tag{27}$$

The forces $\mathbf{f}_I^{\text{LC}}$ and $\mathbf{f}_I^{\text{L}}$ are due to the constraints enforced by the Lagrange multipliers and they are:

$$\begin{aligned}\mathbf{f}_I^{\text{LC}} &= \sum_J \boldsymbol{\lambda}_J^{\text{T}}\frac{\partial \mathbf{g}_J}{\partial \mathbf{u}_I} = \sum_J \boldsymbol{\lambda}_J^{\text{T}}\mathbf{G}_{JI}^{\text{C}},\\ \mathbf{f}_I^{\text{L}} &= \sum_J \boldsymbol{\lambda}_J^{\text{T}}\frac{\partial \mathbf{g}_J}{\partial \mathbf{d}_I} = \sum_J \boldsymbol{\lambda}_J^{\text{T}}\mathbf{G}_{JI}^{\text{M}},\end{aligned} \tag{28}$$

where $N_{IJ} = N_I(\mathbf{X}_J)$ and

$$\mathbf{G}_{JI}^{\text{C}} = \left[\frac{\partial \mathbf{g}_J}{\partial \mathbf{u}_I}\right] = [N_{JI}\mathbf{I}], \quad \mathbf{G}_{JI}^{\text{M}} = \left[\frac{\partial \mathbf{g}_J}{\partial \mathbf{d}_I}\right] = [-\delta_{IJ}\mathbf{I}]. \tag{29}$$

For the augmented Lagrangian method, the discrete equations are

$$\begin{aligned}&\overline{M}_I\ddot{\mathbf{u}}_I = \mathbf{f}_I^{\text{ext C}} - \mathbf{f}_I^{\text{int C}} - \mathbf{f}_I^{\text{ALC}} \quad \text{in } \Omega_0^{\text{C}},\\ &\bar{m}_I\ddot{\mathbf{d}}_I = \mathbf{f}_I^{\text{ext}} - \mathbf{f}_I^{\text{int}} - \mathbf{f}_I^{\text{AL}} \quad \text{in } \Omega_0^{\text{M}},\end{aligned} \tag{30}$$

where $\mathbf{f}_I^{\text{ALC}}$ and $\mathbf{f}_I^{\text{AL}}$ are given by

$$\mathbf{f}_I^{\text{ALC}} = \sum_J \boldsymbol{\lambda}_J^{\text{T}}\frac{\partial \mathbf{g}_J}{\partial \mathbf{u}_I} + \sum_J p\mathbf{g}_J^{\text{T}}\frac{\partial \mathbf{g}_J}{\partial \mathbf{u}_I} = \sum_J \boldsymbol{\lambda}_J^{\text{T}}[N_{IJ}\mathbf{I}] + \sum_J p\left[\sum_I N_{IJ}\mathbf{u}_I - \mathbf{d}_J\right]^{\text{T}}[N_{IJ}\mathbf{I}], \tag{31}$$

$$\mathbf{f}_I^{\text{AL}} = \sum_J \boldsymbol{\lambda}_J^{\text{T}}\frac{\partial \mathbf{g}_J}{\partial \mathbf{d}_I} + \sum_J p\mathbf{g}_J^{\text{T}}\frac{\partial \mathbf{g}_J}{\partial \mathbf{d}_I} = \sum_J \boldsymbol{\lambda}_J^{\text{T}}[-\delta_{IJ}\mathbf{I}] + \sum_J p\left[\sum_I N_{IJ}\mathbf{u}_I - \mathbf{d}_J\right]^{\text{T}}[-\delta_{IJ}\mathbf{I}]. \tag{32}$$

3.3. Explicit algorithm

The Verlet algorithm is used here; it is identical to the central difference method except that the Verlet form avoids half-time-step velocities. This algorithm updates the displacements and velocities at each time step by

$$\mathbf{u}(t+\Delta t) = \mathbf{u}(t) + \dot{\mathbf{u}}(t)\Delta t + \tfrac{1}{2}\ddot{\mathbf{u}}(t)\Delta t^2, \tag{33}$$

$$\dot{\mathbf{u}}(t+\Delta t) = \dot{\mathbf{u}}(t) + \tfrac{1}{2}[\ddot{\mathbf{u}}(t) + \ddot{\mathbf{u}}(t+\Delta t)]\Delta t. \tag{34}$$

To solve the coupled dynamical system with the Lagrange multiplier method, an explicit algorithm was developed based on the velocity Verlet algorithm. Assume that the accelerations, displacements and velocities are known at the time step n. We first obtain the trial displacements at the next time step $n+1$ with the constraints neglected:

$$\begin{aligned}&\mathbf{u}_{I(n+1)}^{*} = \mathbf{u}_{I(n)} + \dot{\mathbf{u}}_{I(n)}\Delta t + \tfrac{1}{2}\ddot{\mathbf{u}}_{I(n)}\Delta t^2 \quad \text{in } \Omega_0^{\text{C}},\\ &\mathbf{d}_{I(n+1)}^{*} = \mathbf{d}_{I(n)} + \dot{\mathbf{d}}_{I(n)}\Delta t + \tfrac{1}{2}\ddot{\mathbf{d}}_{I(n)}\Delta t^2 \quad \text{in } \Omega_0^{\text{M}}\end{aligned} \tag{35}$$

(the subscripts in the parenthesis are the time step number). In the above, the accelerations are obtained from (24) without considering the forces due to the constraints, so

$$\begin{aligned}\ddot{\mathbf{u}}_{I(n+1)} &= \frac{1}{\overline{M}_I}\left[\mathbf{f}^{\text{ext C}}_{I(n+1)} - \mathbf{f}^{\text{int C}}_{I(n+1)}\right] \quad \text{in } \Omega_0^{\text{C}},\\ \ddot{\mathbf{d}}_{I(n+1)} &= \frac{1}{\bar{m}_I}\left[\mathbf{f}^{\text{ext}}_{I(n+1)} - \mathbf{f}^{\text{int}}_{I(n+1)}\right] \quad \text{in } \Omega_0^{\text{M}}.\end{aligned} \tag{36}$$

We then obtain the trial velocities:

$$\begin{aligned}\dot{\mathbf{u}}^*_{I(n+1)} &= \dot{\mathbf{u}}_{I(n)} + \tfrac{1}{2}[\ddot{\mathbf{u}}_{I(n)} + \ddot{\mathbf{u}}_{I(n+1)}]\Delta t \quad \text{in } \Omega_0^{\text{C}},\\ \dot{\mathbf{d}}^*_{I(n+1)} &= \dot{\mathbf{d}}_{I(n)} + \tfrac{1}{2}[\ddot{\mathbf{d}}_{I(n)} + \ddot{\mathbf{d}}_{I(n+1)}]\Delta t \quad \text{in } \Omega_0^{\text{M}}.\end{aligned} \tag{37}$$

The velocities at time step $n+1$ can be alternatively expressed as

$$\begin{aligned}\dot{\mathbf{u}}_{I(n+1)} &= \dot{\mathbf{u}}_{I(n)} + \frac{1}{2}\left[\ddot{\mathbf{u}}_{I(n)} - \overline{M}_I^{-1}\mathbf{f}^{\text{L}}_{I(n)} + \ddot{\mathbf{u}}_{I(n+1)} - \overline{M}_I^{-1}\mathbf{f}^{\text{LC}}_{I(n+1)}\right]\Delta t\\ &= \dot{\mathbf{u}}_{I(n)} + \frac{1}{2}[\ddot{\mathbf{u}}_{I(n)} + \ddot{\mathbf{u}}_{I(n+1)}]\Delta t - \overline{M}_I^{-1}\Delta t\sum_J \mathbf{G}^{\text{C}}_{JI}\boldsymbol{\lambda}_J = \dot{\mathbf{u}}^*_{I(n+1)} - \overline{M}_I^{-1}\Delta t\sum_J \mathbf{G}^{\text{C}}_{JI}\boldsymbol{\lambda}_J,\end{aligned} \tag{38}$$

$$\begin{aligned}\dot{\mathbf{d}}_{I(n+1)} &= \dot{\mathbf{d}}_{I(n)} + \frac{1}{2}\left[\ddot{\mathbf{d}}_{I(n)} - \bar{m}_I^{-1}\mathbf{f}^{\text{L}}_{I(n)} + \ddot{\mathbf{d}}_{I(n+1)} - \bar{m}_I^{-1}\mathbf{f}^{\text{L}}_{I(n+1)}\right]\Delta t\\ &= \dot{\mathbf{d}}_{I(n)} + \frac{1}{2}[\ddot{\mathbf{d}}_{I(n)} + \ddot{\mathbf{d}}_{I(n+1)}]\Delta t - \bar{m}_I^{-1}\Delta t\sum_J \mathbf{G}^{\text{M}}_{JI}\boldsymbol{\lambda}_J = \dot{\mathbf{d}}^*_{I(n+1)} - \bar{m}_I^{-1}\Delta t\sum_J \mathbf{G}^{\text{M}}_{JI}\boldsymbol{\lambda}_J,\end{aligned} \tag{39}$$

where $\boldsymbol{\lambda}_I = \frac{1}{2}[\boldsymbol{\lambda}_{I(n)} + \boldsymbol{\lambda}_{I(n+1)}]$ denote the unknown Lagrange multipliers (a Lagrange multiplier is assigned to each atom). The above velocities satisfy the constraints (19) in time derivative form

$$\dot{\mathbf{g}}_{I(n+1)} = \dot{\mathbf{u}}(\mathbf{X}_I)_{(n+1)} - \dot{\mathbf{d}}_{I(n+1)} = \sum_J N_{IJ}\dot{\mathbf{u}}_{J(n+1)} - \dot{\mathbf{d}}_{I(n+1)}. \tag{40}$$

Substituting (38) and (39) into (40), the unknown Lagrange multipliers can be obtained by solving the following equations:

$$\sum_L \mathbf{A}_{IL}\boldsymbol{\lambda}_L = \mathbf{g}^*_I, \tag{41}$$

where

$$\mathbf{A}_{IL} = \Delta t\overline{M}_I^{-1}\sum_J N_{JI}\mathbf{G}^{\text{C}}_{LJ} - \Delta t\bar{m}_I^{-1}\mathbf{G}^{\text{M}}_{LI}, \tag{42}$$

$$\mathbf{g}^*_I = \sum_J N_{JI}\dot{\mathbf{u}}^*_J - \dot{\mathbf{d}}^*_I. \tag{43}$$

To reduce the computational cost, the matrix $\mathbf{A}$ consisting of submatrices $\mathbf{A}_{IL}$ is diagonalized as a diagonal $n \times n$ matrix where $n = n_{\text{SD}}n_\lambda$; n_{SD} is the number of space dimensions and n_λ the number of Lagrange multipliers. The diagonal matrix is given by

$$\mathbf{A}_{II} = \sum_L\left[\Delta t\overline{M}_I^{-1}\sum_J N_{JI}\mathbf{G}^{\text{C}}_{LJ} - \Delta t\bar{m}_I^{-1}\mathbf{G}^{\text{M}}_{LI}\right]. \tag{44}$$

Therefore, the unknown Lagrange multipliers can be obtained by

$$\boldsymbol{\lambda}_I = \mathbf{A}_{II}^{-1}\mathbf{g}^*_I. \tag{45}$$

Table 1
Explicit algorithm of dynamics solution

1.	Initialize the domains, displacements, velocities and accelerations
2.	Calculate the displacements by Eq. (35)
3.	Calculate the trial velocities by Eq. (37)
4.	Solve Eq. (45) for the unknown Lagrange multipliers
5.	Update the velocities at next time step by Eqs. (38) and (39)
6.	Repeat steps 2–5 until end of simulation

Note that there is no summation on I. After the Lagrange multipliers are obtained, we obtain the corrected velocities at time step $n+1$ by substituting Lagrange multipliers into (38) and (39).

For the augmented Lagrangian method, the accelerations for the trial velocities in (37) are rewritten as

$$\begin{aligned}
\ddot{\mathbf{u}}_{I(n+1)} &= \frac{1}{\overline{M}_I}\left[\mathbf{f}^{\text{ext C}}_{I(n+1)} - \mathbf{f}^{\text{int C}}_{I(n+1)} - \mathbf{f}^{\text{PC}}_{I(n+1)}\right] \quad \text{in } \Omega_0^{\text{C}},\\
\ddot{\mathbf{d}}_{I(n+1)} &= \frac{1}{\bar{m}_I}\left[\mathbf{f}^{\text{ext}}_{I(n+1)} - \mathbf{f}^{\text{int}}_{I(n+1)} - \mathbf{f}^{\text{P}}_{I(n+1)}\right] \quad \text{in } \Omega_0^{\text{M}},
\end{aligned} \tag{46}$$

where $\mathbf{f}_I^{\text{PC}}$ and $\mathbf{f}_I^{\text{P}}$ are the extra forces from the penalty term and are parts of $\mathbf{f}_I^{\text{ALC}}$ and $\mathbf{f}_I^{\text{AL}}$. $\mathbf{f}_I^{\text{PC}}$ and $\mathbf{f}_I^{\text{P}}$ are defined as

$$\begin{aligned}
\mathbf{f}_I^{\text{PC}} &= \sum_J p\left[\sum_I N_{IJ}\mathbf{u}_I - \mathbf{d}_J\right]^{\text{T}}[N_{IJ}\mathbf{I}],\\
\mathbf{f}_I^{\text{P}} &= \sum_J p\left[\sum_I N_{IJ}\mathbf{u}_I - \mathbf{d}_J\right]^{\text{T}}[-\delta_{IJ}\mathbf{I}].
\end{aligned} \tag{47}$$

Otherwise the procedure is the same. A flowchart of the explicit algorithm of dynamics solution for the bridging domain coupling method is shown in Table 1.

Because the scaling parameter α varies between 0 and 1 in the overlapping subdomain, there may be zero-mass nodes along the edge of the continuum domain, Γ_0^{α}, as well as along the edge of the molecular domain, Γ_1^{α}. To solve (45) for the Lagrange multipliers inside the overlapping domain, the scaling parameter α along Γ_0^{α} is replaced by a small value, i.e. 0.001, and along Γ_1^{α}, by $\alpha = 0.999$.

3.4. Multiple-time-step algorithm

One of the issues in multiscale concurrent coupling is in tailoring the time step to the subdomains of the model. If a single time step is used in both the continuum and molecular models, the stable time step depends via the Courant condition on the atomic spacing. Therefore, computations will be wasted in the continuum model. When the finite element mesh is graded down to the atomistic level in the overlapping domain, it is difficult to tailor the time step. We usually use a uniform mesh for the continuum domain, so a larger time step can be used in the continuum model while a fine time step is used in the molecular model. The following describes the multiple-time-step algorithm. This algorithm is based on [24,25]. As shown in Fig. 3, ΔT denotes the coarse time step; Δt denotes the fine time step and $\Delta T = N\Delta t$. The multi-time-step Verlet algorithm then becomes

$$\begin{aligned}
\mathbf{u}_{I(n+1)} &= \mathbf{u}_{I(n)} + \dot{\mathbf{u}}_{I(n)}\Delta T + \tfrac{1}{2}\ddot{\mathbf{u}}_{I(n)}\Delta T^2 \quad \text{in } \Omega_0^{\text{C}},\\
\mathbf{d}_{I\left(n+\frac{j+1}{N}\right)} &= \mathbf{d}_{I\left(n+\frac{j}{N}\right)} + \dot{\mathbf{d}}_{I\left(n+\frac{j}{N}\right)}\Delta t + \tfrac{1}{2}\ddot{\mathbf{d}}_{I\left(n+\frac{j}{N}\right)}\Delta t^2 \quad \text{in } \Omega_0^{\text{M}},
\end{aligned} \tag{48}$$

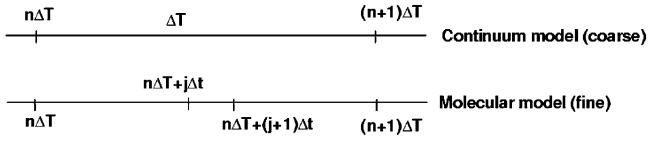

Fig. 3. Arrangement of time steps in multi-time-step algorithm method.

Table 2
Explicit algorithm of dynamics solution

1.	Initialize the domains, displacements, velocities and accelerations
2.	Calculate the displacements of nodes by Eq. (48) at coarse time step
3.	Calculate the displacements of atoms by Eq. (48) at fine time step
4.	Calculate the trial velocities by Eq. (50)
5.	Solve Eq. (45) for the unknown Lagrange multipliers
6.	Update the velocities at next fine time step by Eqs. (51) and (52)
7.	Repeat steps 3–6 until the next coarse time step
8.	Repeat steps 2–7 until the end of the simulation

and

$$\begin{aligned}
\dot{\mathbf{u}}_{I(n+1)} &= \dot{\mathbf{u}}_{I(n)} + \frac{1}{2}\left[\ddot{\mathbf{u}}_{I(n)} + \ddot{\mathbf{u}}_{I(n+1)}\right]\Delta T \quad \text{in } \Omega_0^{\mathrm{C}},\\
\dot{\mathbf{d}}_{I\left(n+\frac{j+1}{N}\right)} &= \dot{\mathbf{d}}_{I\left(n+\frac{j}{N}\right)} + \frac{1}{2}\left[\ddot{\mathbf{d}}_{I\left(n+\frac{j}{N}\right)} + \ddot{\mathbf{d}}_{I\left(n+\frac{j+1}{N}\right)}\right]\Delta t \quad \text{in } \Omega_0^{\mathrm{M}},
\end{aligned} \tag{49}$$

where $0 \leqslant j < N$.

In the explicit algorithm described in the previous section, the velocities of nodes and atoms in the overlapping domain are corrected by the constraints. In the multi-time-step method, the constraints are applied at every fine time step. The trial velocities corresponding to (37) are computed by

$$\begin{aligned}
\dot{\mathbf{u}}^{*}_{I\left(n+\frac{j+1}{N}\right)} &= \dot{\mathbf{u}}_{I\left(n+\frac{j}{N}\right)} + \frac{1}{2}\left[\ddot{\mathbf{u}}_{I(n)} + \ddot{\mathbf{u}}_{I(n+1)}\right]\Delta t \quad \text{in } \Omega_0^{\mathrm{C}},\\
\dot{\mathbf{d}}^{*}_{I\left(n+\frac{j+1}{N}\right)} &= \dot{\mathbf{d}}_{I\left(n+\frac{j}{N}\right)} + \frac{1}{2}\left[\ddot{\mathbf{d}}_{I\left(n+\frac{j}{N}\right)} + \ddot{\mathbf{d}}_{I\left(n+\frac{j+1}{N}\right)}\right]\Delta t \quad \text{in } \Omega_0^{\mathrm{M}},
\end{aligned} \tag{50}$$

where $\mathbf{u}_{I\left(n+\frac{j}{N}\right)}$ is the nodal displacement which is already corrected from the last fine time step. Note that the accelerations are unchanged during the coarse time step ΔT while the velocities of nodes are updated every fine time step Δt. The corrected velocities for next fine time step are:

$$\dot{\mathbf{u}}_{I\left(n+\frac{j+1}{N}\right)} = \dot{\mathbf{u}}^{*}_{I\left(n+\frac{j+1}{N}\right)} - \overline{M}_I^{-1}\Delta t \sum_J \mathbf{G}^{\mathrm{C}}_{JI}\boldsymbol{\lambda}_J \quad \text{in } \Omega_0^{\mathrm{C}}, \tag{51}$$

$$\dot{\mathbf{d}}_{I\left(n+\frac{j+1}{N}\right)} = \dot{\mathbf{d}}^{*}_{I\left(n+\frac{j+1}{N}\right)} - \bar{m}_I^{-1}\Delta t \sum_J \mathbf{G}^{\mathrm{M}}_{JI}\boldsymbol{\lambda}_I \quad \text{in } \Omega_0^{\mathrm{M}}. \tag{52}$$

Table 2 shows the flow chart of the multiple-time-step algorithm.

4. Coupling to heat conduction

When temperature effects are important in a problem, it is necessary to couple the energy equation (10) in the continuum to the molecular dynamics model. The energy equation is not needed in the molecular

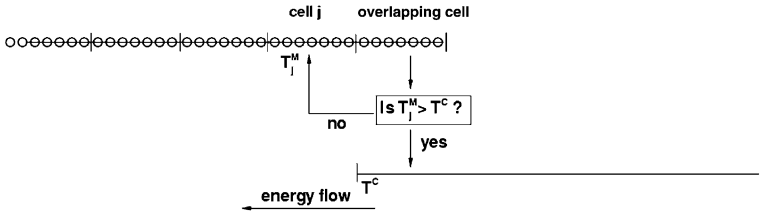

Fig. 4. Heat conduction in 1D with bridging domain coupling method.

subdomain; heat flow and the second law of thermodynamics are inherent in the discrete equations. The bridging domain method lends itself naturally to such coupling of thermal flow because the overlapping domain provides an entity for affecting the energy transfer.

The basic idea of the coupling is shown in Fig. 4. The molecular domain is subdivided into cells as shown. The temperature in each cell is defined by

$$T = \frac{2K_e}{knN}, \tag{53}$$

where n is the number of the space dimension; N is the number of atoms in the cell; k is the Boltzmann constant and K_e is the kinetic energy of the cell.

Since the projection always removes energy from the fine scale, it provides the source of energy for the continuum energy equation. The energy lost in each time step is given by

$$E_T = \sum_I^{N_M^{int}} \left(\dot{\mathbf{d}}_I^T \Delta t \sum_J \mathbf{G}_{JI}^M \boldsymbol{\lambda}_J \right) - \sum_I^{N_C^{int}} \left(\dot{\mathbf{u}}_I^T \Delta t \sum_J \mathbf{G}_{JI}^C \boldsymbol{\lambda}_J \right), \tag{54}$$

where N_M^{int} and N_C^{int} are the numbers of molecules and nodes, respectively.

However, as shown in the figure, to observe the second law of thermodynamics, a switch must be included so that energy is transferred to the continuum domain only when the temperature of the adjacent molecular domain is greater than that of the left hand end of continuum T^C. If $T^C > T^M$, the energy lost by the projection is transferred back to the molecular domain.

5. Examples

5.1. Application of bridging domain coupling method in 1D

In the 1D examples, we used the Lennard-Jones (LJ) 6-12 interatomic potential [26]. This potential is expressed as

$$W^M(r_{ij}) = 4\varepsilon \left[\left(\frac{\sigma}{r_{ij}} \right)^{12} - \left(\frac{\sigma}{r_{ij}} \right)^{6} \right], \tag{55}$$

where ε and σ are parameters. Here we use $\varepsilon = 0.2J$ and $\sigma = 0.11$ nm so that the equilibrium bond length is $r_0 = 0.139$ nm. The interatomic force for bond r_{ij} is the negative of the first derivative of the potential with respect to r_{ij}:

$$f(r_{ij}) = -\frac{\partial W^M(r_{ij})}{\partial r_{ij}} = 48\varepsilon \frac{\sigma^{12}}{r_{ij}^{13}} - 24\varepsilon \frac{\sigma^6}{r_{ij}^7}. \tag{56}$$

In the continuum model, similar to the quasicontinuum method [21], the first Piola–Kirchhoff stress P is obtained by differentiating the potential energy density with respect to the continuum deformation gradient F, giving:

$$P = \frac{\partial W^{C}(F)}{\partial F} = \frac{24\varepsilon}{r_0}\left[\frac{(\sigma r_0)^6}{F^7} - \frac{2(\sigma r_0)^{12}}{F^{13}}\right], \tag{57}$$

where $F = r/r_0$.

The entire domain is 60.0 nm in length and there are 211 atoms in the molecular domain. The continuum domain contains 40 elements of equal length. The time step is 0.002 ps. In the bridging domain coupling method, an overlapping subdomain links the molecular and continuum domains, as shown in Fig. 5. Various sizes of the overlaps were studied.

Our test problems are similar to [8]. We apply initial displacements on the atoms at the left-end portion of the molecular domain. The initial displacements contain a combination of high frequency and low frequency modes as shown in Fig. 6. We will study how the high frequency and low frequency waves propagate through the molecular domain and pass into the continuum domain.

We first study the behavior of the model for different lengths of the overlapping subdomain. Fig. 7 shows the displacements in the entire domain at time $t = 2.4$ ps for two different lengths of the overlapping domain, 9 and 3 nm, which correspond to 9 and 3 elements respectively. We can see that spurious wave reflections are almost completely eliminated for the 9 nm overlapping subdomain. For the 3 nm overlapping subdomain, a portion of the high frequency wave is reflected by the interface between the molecular and continuum domains although it has been weakened.

To illustrate this more clearly, we also plot the evolution of energy with time in Fig. 8. Fig. 8(a) shows the time history of the molecular energy, which is the sum of kinetic and potential energies, in the molecular domain, while Fig. 8(b) gives the time history of the continuum energy. The energy of the low frequency

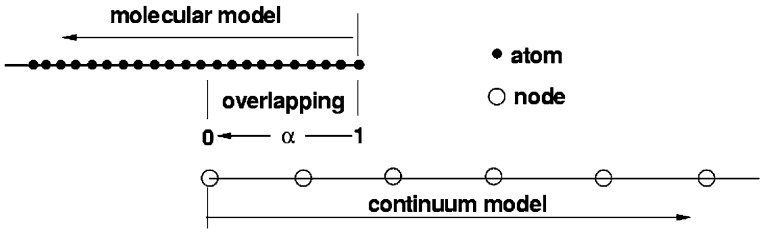

Fig. 5. Overlapping domain decomposition method in 1D.

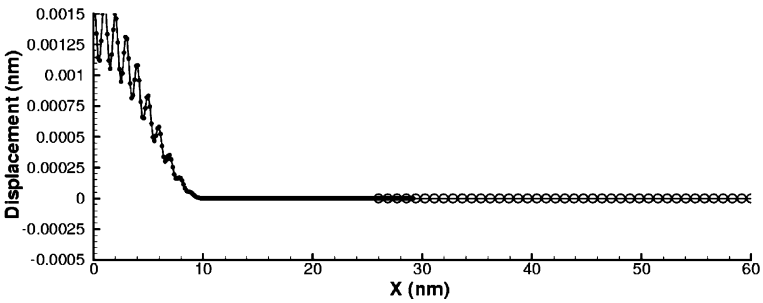

Fig. 6. Initial displacements applied on the atoms.

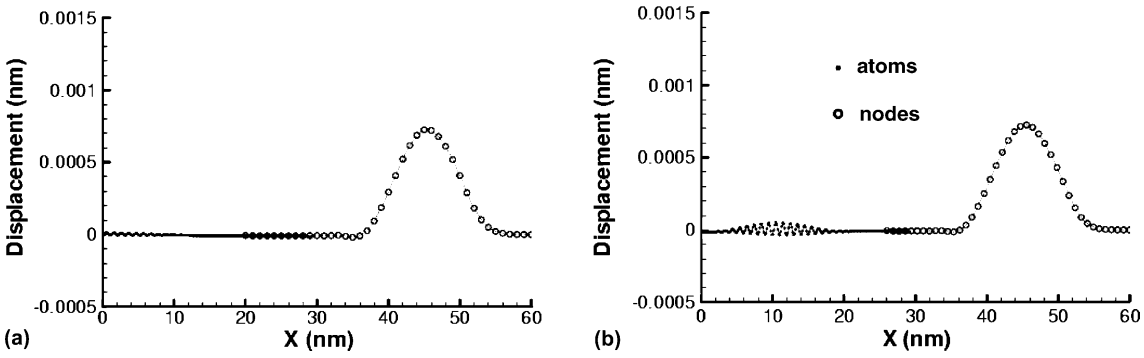

Fig. 7. Displacements with different lengths of overlapping subdomain at $t = 2.4$ ps: (a) 9 nm overlapping subdomain; (b) 3 nm overlapping subdomain.

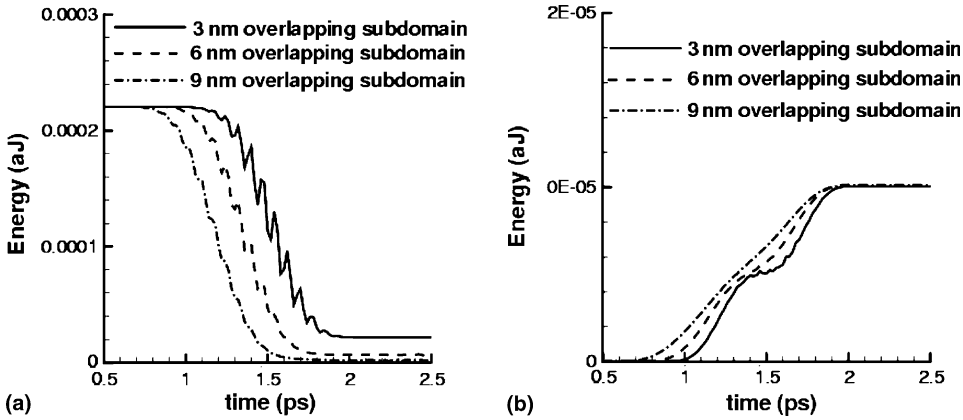

Fig. 8. Time history of energy: (a) molecular model; (b) continuum model.

wave is 5% of the total energy and it can be seen from Fig. 8(b) that all of this energy passes into the continuum domain regardless of the size of the overlapping subdomain. On the other hand, we found our bridging domain coupling can dramatically reduce the spurious wave reflections. Even for a small (3 nm) overlapping subdomain as in Fig. 8(a), only 10% of total energy is reflected back into the molecular domain. As the size of overlapping subdomain increases, the spurious wave reflection decreases. For the 6 nm length overlapping subdomain, only 3% of total energy remains in the molecular subdomain. If the overlapping subdomain is big enough, such as 9 nm in this problem, the spurious wave reflection is almost completely eliminated and almost no energy remains in the molecular subdomain.

For comparison, consider an edge-to-edge coupling method, where the continuum domain and molecular domain are attached to each other at a single node, as shown in Fig. 9. On the interface of molecular/continuum domain, the motion of the atom I is constrained to the motion of the node I, i.e.

$$g = d_I - u_I = 0. \tag{58}$$

The initial displacements are applied on the atoms as before. From Fig. 10, we can see that the high frequency part of the wave is largely reflected by the molecular/continuum interface.

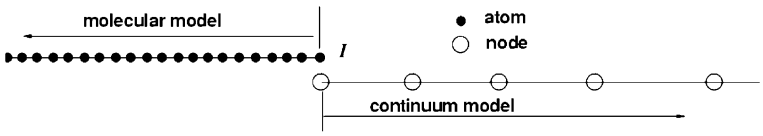

Fig. 9. Edge-to-edge coupling model in one dimension.

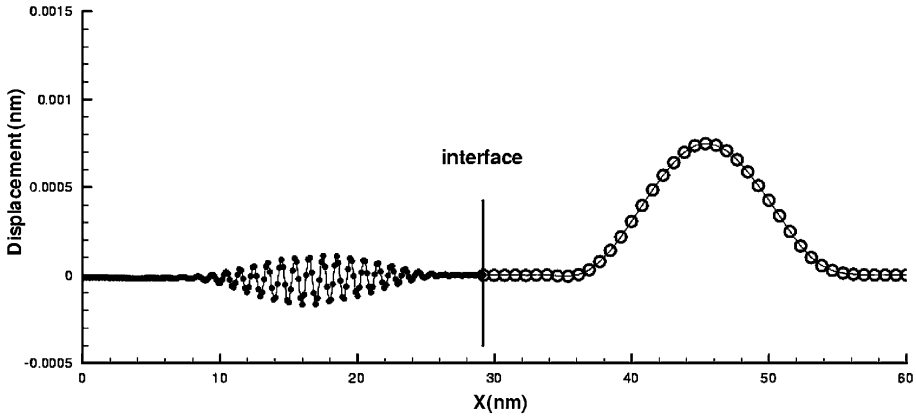

Fig. 10. Spurious wave reflection with edge-to-edge coupling at $t = 2.4$ ps.

5.2. Wave propagation with bilinear force-deflection law

Next we consider a potential with a nonlinear law for wave propagation in a rod. The potential function is shown in Fig. 11 and its force-deflection relation is a bilinear function. k is the first stiffness and the second stiffness $k_p = 0.25k$. An increasing load is applied on one end of the rod and kept constant beyond the threshold force f_0. If the applied load is increased slowly, we are able to observe that two step waves that propagate with two different wave speeds.

Both the bridging domain method and edge-to-edge coupling method are used to simulate the wave propagating from molecular domain to continuum domain. Fig. 12 shows the configurations when the stress waves pass through the continuum domain. Due to the numerical method, there are some oscillations behind the wave fronts compared to the theoretical analysis. We can see that bridging domain does not distort the wave and there is no evidence of spurious reflections. However, edge-to-edge coupling method obviously distorts the wave due to the spurious reflections.

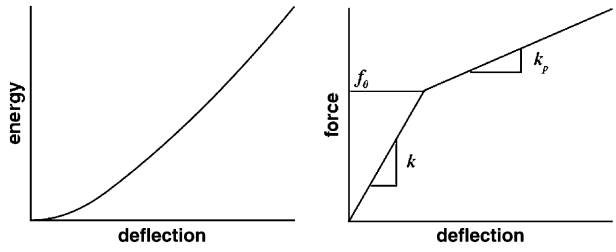

Fig. 11. Bilinear force-deflection law.

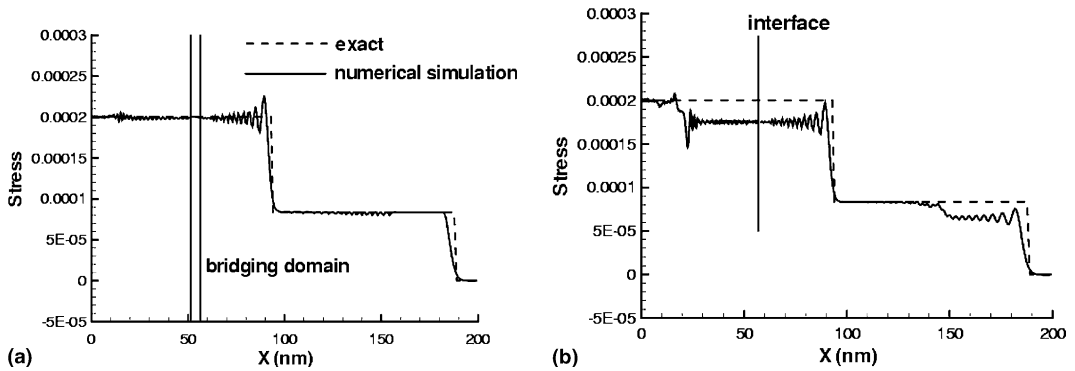

Fig. 12. Wave propagation with bilinear force-deflection law: (a) bridging domain method; (b) edge-to-edge coupling method.

5.3. Application of bridging domain coupling method with multiple time steps

Because we can use much larger elements in the continuum domain, the multi-time step method is well suited to the bridging domain method. In this problem, the coarse time step is 10 times the fine time step, i.e. $\Delta T = 10\Delta t$, where $\Delta t = 0.002$ ps as before. Fig. 13 shows the displacements for the entire domain after a wave has passed into the continuum when multi-time step integration is used. We can see that the spurious wave reflection is eliminated and the time history of the molecular energy is almost identical to that from single time step simulation shown in Fig. 14.

Since the stable large time step depends only on the size of the elements in the continuum model, if we increase the size of the elements, we can use a larger time step in the continuum model. Here, we use 21 nodes in the continuum domain and the coarse time step is 20 times the fine time step i.e. $\Delta T = 20\Delta t$. Fig. 15 shows the displacements at $t = 2.4$ ps and the time history of the molecular energy for multiple-time-step integration compared with that obtained with a uniform time step (Fig. 16). It can be seen that the displacements are almost identical to the results when $\Delta T = 10\Delta t$ (Fig. 13) and little energy remains in the molecular subdomain.

5.4. Application of bridging domain coupling method in 2D

We consider wave propagation in a graphene sheet, which is 12.0378 nm in width and 60.0 nm in length. There are 14,140 atoms in the molecular model as well as 226 nodes in the continuum model,

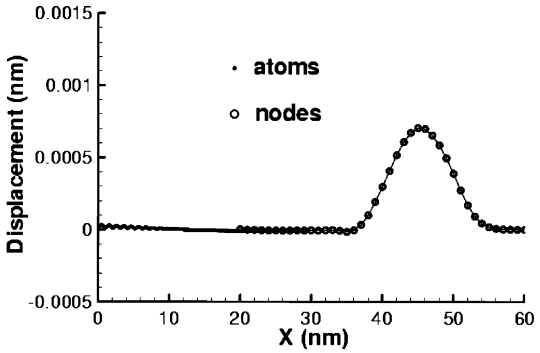

Fig. 13. Displacements at $t = 2.4$ ps for $\Delta T = 10\Delta t$.

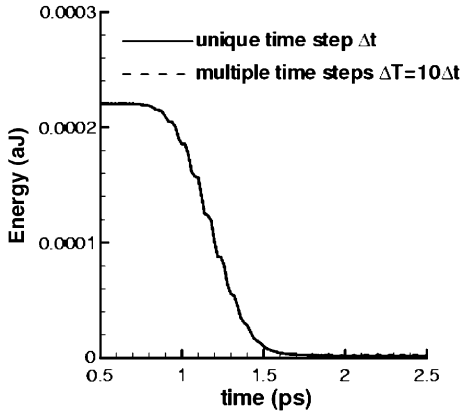

Fig. 14. Time history of molecular energy for $\Delta T = 10\Delta t$.

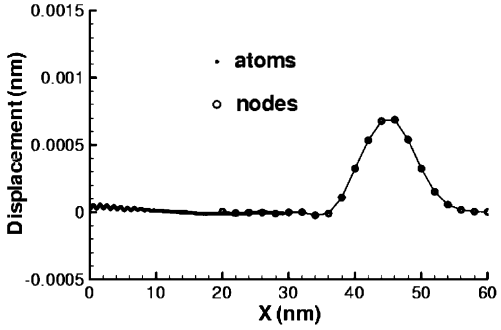

Fig. 15. Displacements at $t = 2.4$ ps for $\Delta T = 20\Delta t$.

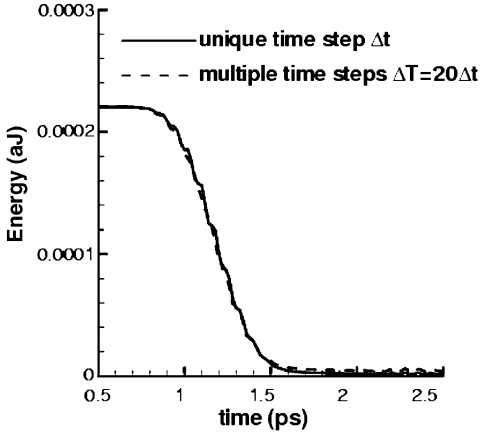

Fig. 16. Time history of molecular energy for $\Delta T = 20\Delta t$.

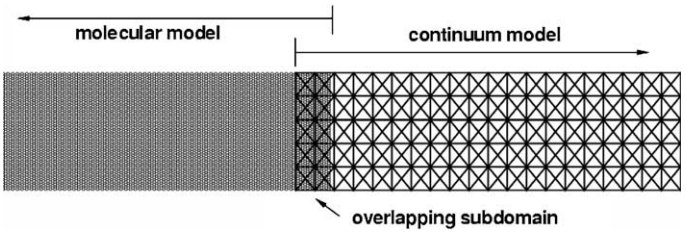

Fig. 17. Bridging domain coupling method application in 2D.

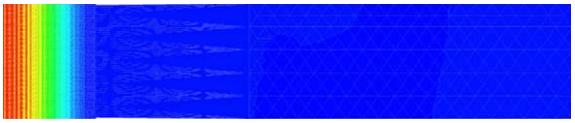

Fig. 18. Initial plane wave in graphene sheet.

as shown in Fig. 17. Fig. 18 shows the initial plane wave, which is a combination of high frequency and low frequency waves; a sliding boundary condition is applied on the top and bottom of the sheet. The potential function is a modified Morse potential [27]:

$$\begin{aligned} &w_{\mathrm{M}}(\mathbf{x}_I, \mathbf{x}_J) = E_{\mathrm{stretch}} + E_{\mathrm{angle}}, \\ &E_{\mathrm{stretch}} = D_{\mathrm{e}}\{[1 - \mathrm{e}^{-\beta(r-r_0)}]^2 - 1\}, \\ &E_{\mathrm{angle}} = \tfrac{1}{2}k_\theta(\theta - \theta_0)^2[1 + k_{\mathrm{sextile}}(\theta - \theta_0)^4], \end{aligned} \tag{59}$$

where E_{stretch} is the bond energy due to bond stretch, while E_{angle} is the bond energy due to bond angle bending. r is the length of the bond, and θ is the current angle of the adjacent bond, a standard deformation measure in molecular mechanics. The parameters are

$$r_0 = 1.39 \times 10^{-10}\ \mathrm{m}, \quad D_{\mathrm{e}} = 6.03105 \times 10^{-19}\ \mathrm{N\,m}, \quad \beta = 2.625 \times 10^{10}\ \mathrm{m}^{-1},$$

$$\theta_0 = 2.094\ \mathrm{rad}, \quad k_\theta = 0.9 \times 10^{-18}\ \mathrm{N\,m/rad}^2, \quad k_{\mathrm{sextile}} = 0.754\ \mathrm{rad}^{-4}.$$

We first study the behavior of the model with a small overlapping subdomain 3 nm in length. We find that spurious wave reflection can be reduced as in 1D and only 10% of total energy is left in molecular model. As we described before, a parameter α is introduced in the overlapping subdomain and is defined by the linear form i.e. $\alpha = l(\mathbf{X})/l_0$, see Fig. 2. We have found that the spurious wave reflection will be reduced more effectively if a nonlinear relation is used for the parameter: $\alpha = [l(\mathbf{X})/l_0]^\gamma$. For $\gamma = 0.25$ the energy in the molecular model is reduced to 6.5%. Fig. 19 shows the energy history of the molecular model.

For a larger overlapping subdomain, which is 9 nm of length, we obtain less spurious wave reflection. Only 2% of the total energy is left as shown in Fig. 20(a). As in the results we obtained in 1D applications, Fig. 20(b) shows that regardless of the size of the overlapping subdomain, the energies which pass into the continuum model are identical. Fig. 21 shows the displacements at time $t = 2.4$ ps.

5.5. Cylindrical wave propagation

We use the same potential function as in Section 5.4. The coupled model for this problem is shown as Fig. 22; it consists of 25,656 atoms in molecular model and 3192 nodes in continuum model. The initial

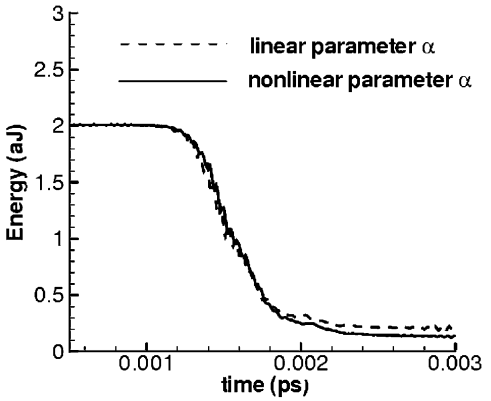

Fig. 19. The energy history of molecular model with 3 nm length of overlapping subdomain.

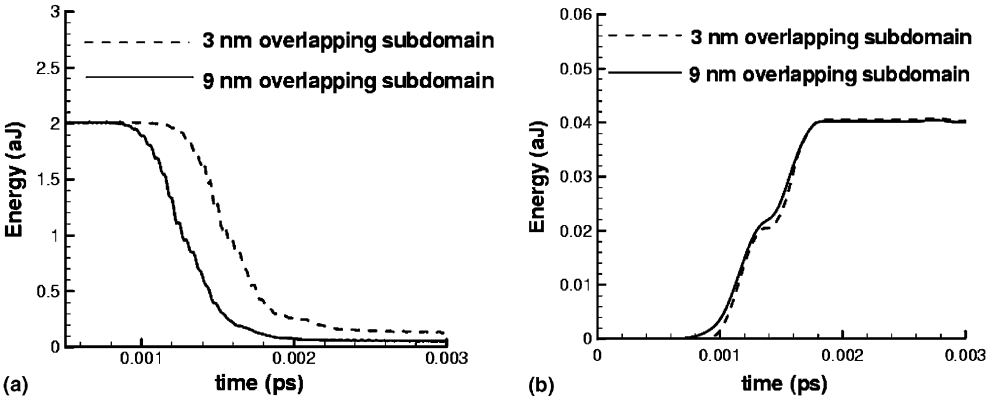

Fig. 20. The comparison of energy histories for overlapping domains of two sizes: (a) molecular model; (b) continuum model.

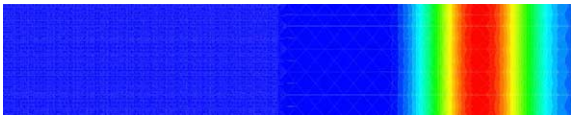

Fig. 21. Contour plot of displacements at $t = 2.4$ ps.

velocities are applied on the atoms around the inner circle. It is a combination of high frequency waves and a low frequency wave. When the cylindrical wave passes by the bridging domain, only 2% of the energy is left in the molecular domain as shown in Fig. 23. The contour plots of the velocities are shown in Fig. 24.

5.6. Heat transfer in 1D

We study heat transfer in 1D rod with the bridging domain coupling model. The specific heat $\bar{c}$ and heat conductivity κ are defined by

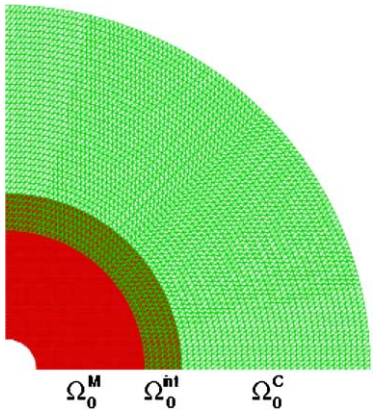

Fig. 22. Bridging domain coupling model.

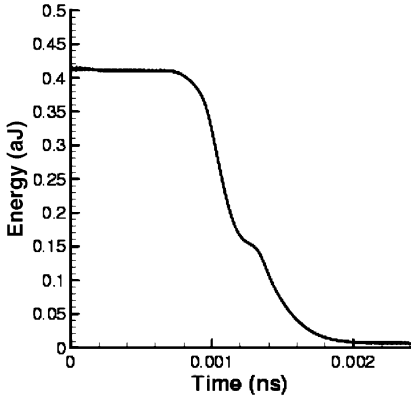

Fig. 23. History of energy in molecular domain.

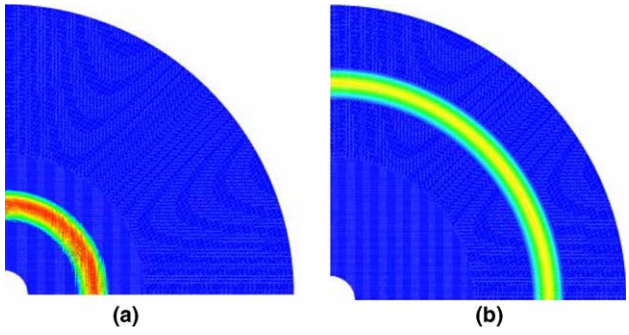

Fig. 24. Cylinder wave propagation: (a) $t = 0.4$ ps; (b) $t = 1.2$ ps.

$$\bar{c} = \frac{\mathrm{d}u}{\mathrm{d}T}, \quad \kappa = \frac{h}{\mathrm{d}T/\mathrm{d}X}, \tag{60}$$

where u is the internal energy and h is the heat flux. We first obtained $\bar{c}$ and κ for the molecular model by considering a one-dimensional model of 3900 atoms. Two heat baths [28] are added on the ends of the system and the temperatures of the baths are 300 and 700 K, respectively. The values of specific heat and heat conductivity were obtained as follows. We applied a heat source with a constant energy rate at the left end and a prescribed temperature at the right end; both conditions were applied to one-dimensional cells of 100 atoms. The model was then run until equilibrium was achieved. The slope of the temperature field and the temperature at the left hand cell was then used to obtain the specific heat and conductivity by a Fourier model of heat conduction, which gives

$$\bar{c} = \frac{\mathrm{d}u}{\mathrm{d}T} = 10.0\ \mathrm{J\,K\,g^{-1}}, \quad \kappa = \frac{h}{\mathrm{d}T/\mathrm{d}X} = 37.4\ \mathrm{J\,s^{-1}\,m^{-1}\,K^{-1}}. \tag{61}$$

Note that the effects of heat waves were neglected in this estimate of the thermal properties.

The rod is subdivided into 39 cells consisting of 100 atoms. The temperature is defined by

$$T = \frac{2\alpha}{knN}\left[\sum_{I=1}^{N}\frac{p_I p_I}{2m_I}\right] + \frac{(1-\alpha)}{2knN}\left[\sum_{I} M_I \mathbf{v}_I^2\right], \tag{62}$$

where n is the number of the space dimensions, N is the number of atoms in the cell and k is the Boltzmann constant. Note that the temperature in the continuum subdomain includes the kinetic energy of the continuum. This is quite important when the size of the continuum element is only moderately larger than the lattice spacing (e.g. $3l$ to $10l$), since a substantial part of the temperature may be reflected in its kinetic energy.

The coupled method is described in Section 4. The parameters of Eq. (61) are used in the heat equation (energy equation) in the continuum model:

$$\rho\bar{c}\frac{\partial T}{\partial t} = \kappa\frac{\partial^2 T}{\partial x^2}. \tag{63}$$

Fig. 25 shows the temperature distribution for the coupled model compared with the results from molecular dynamics and the exact solution of (63). Some anomalies are apparent in the temperature in the cells adjacent to the ends: the left-hand temperature drops next to the end, whereas at the right-hand end, the temperature is significantly above a linear field. These may be due to Kapitza effects. The energy flows into the system for coupled calculation and the molecular dynamics calculation are compared in Fig. 26. They show almost perfect agreement. As a next test of the method, the end conditions were reversed, so that the heat flows from the continuum subdomain to the molecular subdomain. The temperature fields are shown in Fig. 27. Again, the agreement is quite good.

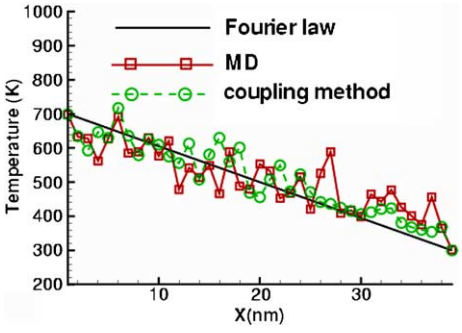

Fig. 25. Temperature distribution along the system.

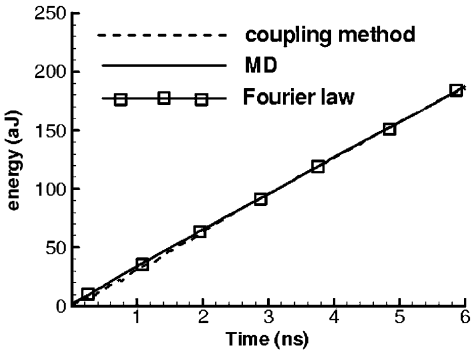

Fig. 26. Energies flow in the system.

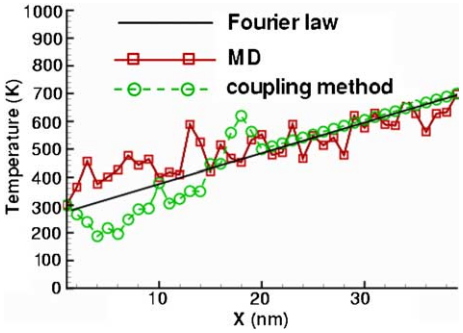

Fig. 27. Temperature distribution with revised energy flowing.

5.7. Dynamic crack propagation in a graphene sheet

We consider the growth of an initial crack in a graphene sheet. A modified Morse potential [27] is used for the carbon bond. Using the analytical approach given in [29], Young's modulus for the graphene sheet is 0.9 TPa and Poisson's ratio is 0.29. The density of graphene sheet, ρ, is 7.9387e−7 kg/m^2. Therefore, the shear wave speed is $C_s = 12,223$ m/s; the dilatational wave speed is $C_d = 22474.9$ m/s, and the Rayleigh wave speed is $C_R = 11316.7$ m/s.

We consider a graphene sheet of 48,240 atoms with a central crack that is 4 nm long, as shown in Fig. 28. The left-hand edge is a plane of symmetry. On the upper side of the model, the velocity is prescribed to be 86.8 m/s, and the lower edge is fixed. The initial temperature was taken to be 0 K. The complete model with finite elements is of size 24 nm$\times$48 nm; 0.002 ns is required for the waves from the crack tip to reach the outer boundary and reflect back. Therefore, the model is only adequate for that time frame. This time interval could be increased substantially by adding a silent boundary around the edge of the finite element model, but this has not been done yet.

The crack is shown at $t = 0.016$ ns in Fig. 29. At $t = 0.0151$ ns, the crack starts to propagate at 3200.0 m/s. We observed that the speed of crack tip increases as the crack propagates. Towards the end of the simulation, the speed of crack reaches a steady value of 8025.0 m/s, which is about 71% of the Raleigh wave speed. This is somewhat higher than experimental observations and finite element simulations of continua, see [30]. Fig. 30 shows the crack speed after the crack starts growing as a function of time.

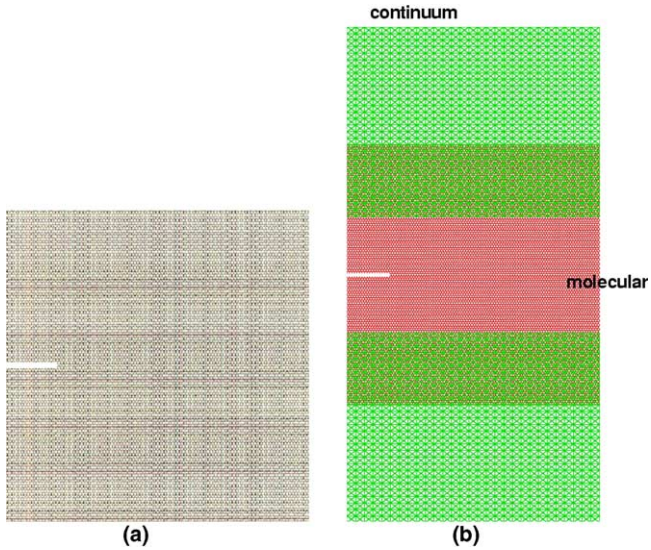

Fig. 28. (a) Molecular model and (b) complete coupled model of graphene sheet.

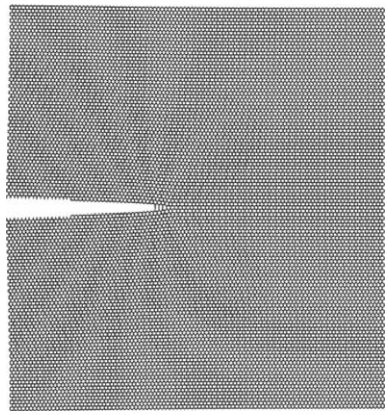

Fig. 29. Crack propagation in a graphene sheet at $t = 0.016$ ns.

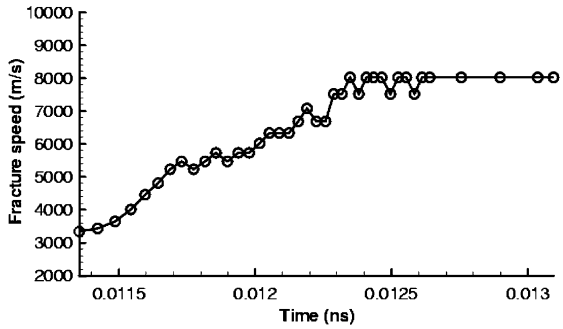

Fig. 30. Speed of crack increasing with time until a steady value.

We also considered different prescribed velocities, and we found that the crack started to propagate earlier when a larger prescribed velocity was applied. However, the final speeds of crack propagation were around 8025.0 m/s regardless of what prescribed velocity was applied.

6. Conclusions

A multiscale coupling method has been developed based on a bridging subdomain. In the bridging subdomain coupling method, an overlapping subdomain consisting of the molecular and continuum models is used. A Lagrange multiplier method or augmented Lagrangian method is applied for enforcing the kinematic constraints in the overlapping subdomain. A scalar parameter is used to scale the Hamiltonian in the overlapping subdomain; the total Hamiltonian is a linear combination of the molecular and continuum Hamiltonians. An explicit algorithm for dynamics is developed.

We find that our bridging domain coupling method can dramatically reduce spurious wave reflections at the interface. If the overlapping subdomain is large enough, the high frequency wave reflection is almost completely eliminated. However, good results are also obtained for moderate overlaps if a nonlinear scalar parameter is used in the overlapping subdomain. We have also developed a multi-time step variant of the methods and obtained good results with it.

The bridging domain method also provides a natural way for coupling the molecular model to the energy equation in the continuum. Removal of the energy at a single layer of atoms would undoubtedly result in severe anomalies. Even with the bridging domain, some Kapitza effects are apparent, but they are not severe.

Acknowledgements

We gratefully acknowledge the grant support from the NASA University Research, Engineering and Technology Institute on Bio Inspired Materials (BIMat) under award no. NCC-1-02037 and the Army Research Office.

References

[1] E.B. Tadmor, R. Phillips, M. Ortiz, Hierarchical modeling in the mechanics of materials, Int. J. Solids Struct. 37 (2000) 379–389.
[2] J.R. Doll, D.R. Dion, Generalized Langevin equation approach for atom/solid-surface scattering: numerical techniques for Gaussian generalized Langevin dynamics, J. Chem. Phys. 65 (1976) 3762–3766.
[3] S.A. Adelman, J.D. Doll, Generalized Langevin equation approach for atom/solid surface scattering: general formulation for classical scattering off harmonic solids, J. Chem. Phys. 64 (1976) 2375–2388.
[4] N. Holmes, T. Belytschko, Postprocessing of finite element transient response calculations by digital filters, Comput. & Structures 6 (1976) 211–216.
[5] F. Abraham, J. Broughton, N. Bernstein, E. Kaxiras, Spanning the continuum to quantum length scales in a dynamic simulation of brittle fracture, Europhys. Lett. 44 (1998) 783–787.
[6] J. Broughton, F. Abraham, N. Bernstein, E. Kaxiras, Concurrent coupling of length scales: methodology and application, Phys. Rev. B 60 (1999) 2391–2403.
[7] R.E. Rudd, J.Q. Broughton, Coarse-grained molecular dynamics and the atomic limit of finite elements, Phys. Rev. B 58 (1998) R5893–R5896.
[8] G.J. Wagner, W.K. Liu, Coupling of atomic and continuum simulations using a bridging scale decomposition, J. Comput. Phys. 190 (2003) 249–274.
[9] W. Cai, M. de Koning, V. Bulatov, S. Yip, Minimizing boundary reflections in coupled-domain simulations, Phys. Rev. Lett. 85 (2000) 3213–3216.
[10] Z. Huang, W. E, Matching conditions in atomistic-continuum modeling of materials, Phys. Rev. Lett. 87 (2001) 135501.

[11] E.G. Karpov, G.J. Wagner, W.K. Liu, A Green's function approach to deriving wave-transmitting boundary conditions in molecular dynamics simulations, Comput. Mater. Sci., accepted for publication.
[12] T. Belytschko, S.P. Xiao, Coupling methods for continuum model with molecular model, J. Mult. Comput. Engrg. 1 (2003) 115–126.
[13] W.A. Curtin, R.E. Miller, Atomistic/continuum coupling in computational materials science, Model. Simul. Mater. Sci. Engrg. 11 (2003) R33–R68.
[14] T. Belytschko, R.W. Mullen, Mesh partitions of explicit–implicit time integration, in: J. Bathe et al. (Eds.), Formulations and Computational Algorithms in Finite Element Analysis, MIT Press, 1977.
[15] T. Belytschko, N.D. Gilbersen, Implementation of mixed time integration techniques on a vectorized computer with shared memory, Int. J. Numer. Methods Engrg. 35 (1992) 1803–1828.
[16] C. Farhat, M. Lesoinne, Two efficient staggered algorithms for the serial and parallel solution of three-dimensional nonlinear transient aeroelastic problems, Comput. Methods Appl. Mech. Engrg. 182 (2000) 499–515.
[17] W.K. Liu, J.I. Lin, Stability of mixed time integration schemes for transient thermal analysis, Numer. Heat Trans. J. 5 (1982) 211–222.
[18] T. Belytschko, D. Organ, Y. Krongauz, A coupled finite element-element-free Galerkin method, Comput. Mech. 17 (1996) 186–195.
[19] H. Ben Dhia, Multiscale mechanical problems: the Arlequin method, C. R. Acad. Sci., Paris 326 (Ser-II b) (1998) 899–904.
[20] T. Belytschko, W.K. Liu, B. Moran, Nonlinear Finite Elements for Continua and Structures, Wiley, New York, 2000.
[21] E. Tadmor, M. Ortiz, R. Phillips, Quasicontinuum analysis of defects in solids, Philos. Mag. A 73 (1996) 1529–1563.
[22] M. Arroyo, T. Belytschko, An atomistic-based finite deformation membrane for single layer crystalline films, J. Mech. Phys. Solids 50 (2002) 1941–1977.
[23] D.Y. Tzou, Macro- to Microscale Heat Transfer: the Lagging Behavior, Taylor and Francis, 1997.
[24] T. Belytschko, R. Mullen, Stability of explicit–implicit mesh partitions in time integration, Int. J. Numer. Methods Engrg. 12 (1978) 575–586.
[25] A. Gravouil, A. Combescure, Multi-time-step explicit–implicit method for non-linear structural dynamics, Int. J. Numer. Methods Engrg. 50 (2001) 199–225.
[26] L.A. Girifalco, R.A. Lad, Energy of cohesion, compressibility and the potential energy functions of the graphite system, J. Chem. Phys. 25 (1956) 693–697.
[27] T. Belytschko, S.P. Xiao, G.C. Schatz, R.S. Ruoff, Atomistic simulations of nanotube fracture, Phys. Rev. B 65 (2002).
[28] H.J.C. Berendsen, J.P.M. Postma, W.F. van Gunsteren, A. DiNola, J.R. Haak, Molecular dynamics with coupling to an external bath, J. Chem. Phys. 81 (1984) 3684–3690.
[29] M. Arroyo, T. Belytschko, Finite crystal elasticity of carbon nanotubes based on the exponential Cauchy–Born rule, Phys. Rev. B, in press (2004).
[30] T. Belytschko, H. Chen, J. Xu, G. Zi, Dynamic crack propagation based on loss of hyperbolicity and a new discontinuous enrichment, Int. J. Numer. Methods Engrg. 58 (2003) 1873–1905.